Buckling and Postbuckling Behaviour of Glare Laminates Containing Splices and Doublers. Part 2: Numerical Modelling

Ahmad S.M. Al-Azzawi[a,c,*], Luiz F. Kawashita[b], Carol A. Featherston[a]

[a] *Cardiff School of Engineering, Cardiff University, The Parade, Cardiff CF24 3AA, UK.*
[b] *Advanced Composites Centre for Innovation and Science (ACCIS), University of Bristol, University Walk, Bristol BS8 1TR, UK.*
[c] *College of Engineering, University of Babylon, Babylon, Iraq.*

Abstract

A 3D finite element model using cohesive elements and continuum (bulk) material damage models was developed to examine the progressive damage and failure behaviour of Glare® Fibre Metal Laminate (FML) specimens subjected to in-plane compressive loading. The specimens contained internal 'splice' and 'doubler' features and were either pristine or contained simulated manufacturing defects in the form of artificial delaminations. The initiation and growth of delaminations at the inter-laminar interfaces, damage in the glass fibre reinforced polymer (GFRP) plies, ductile damage in the resin pockets (FM94 epoxy) and the onset of plasticity in the metal layers were examined. Geometric imperfections and load eccentricity were incorporated in an explicit dynamic nonlinear analysis implemented in the software Abaqus/Explicit. A series of buckling tests on specimens with and without artificial delaminations were conducted for validation, which are described in detail in a companion paper. Tests were monitored using Digital Image Correlation (DIC) for visualisation of full-field displacements and strains whilst Acoustic Emission (AE) monitoring enabled detection and localisation of the onset and progression of damage. Results for 'Glare 4B' specimens incorporating longitudinal and transverse delaminations into both splice and doubler geometries are presented. These results revealed that in order for the finite element analyses to be validated, all the damage and plasticity mechanisms

*Corresponding author. Email address: Al-AzzawiAS@cardiff.ac.uk

described above need to be accounted for, as well as load eccentricity and geometry imperfections.

Keywords:
Glare, Buckling, Postbuckling, Delamination, Cohesive Zone Model, Acoustic Emission

---

1. Introduction

The Fibre-Metal Laminate (FML) Glare® is a hybrid material consisting of bonded thin aluminium sheets and glass-fibre reinforced polymer (GFRP) plies made with a toughened epoxy matrix. This material is known for its fatigue resistance and high damage tolerance, in addition to its light weight and resulting high specific properties in comparison to metals. Because of these advantages its use has increased in industries such as the aerospace industry where weight is critical.

In applications such as the A380 fuselage, large panels are needed requiring the use of joints. Two types are commonly used - the 'splice' and the 'doubler' configurations shown in Figure 1 [1]. A splice is formed when aluminium sheets are placed side by side with gaps in between. The gaps are staggered through the thickness such that the fibre layers can provide load transfer to prevent loss of strength. Additional layers can be added internally or externally to further reduce stresses - these are known as doublers.

Whilst enabling the manufacture of larger panels, these features involve additional manufacturing processes which have the potential to introduce defects. This in addition to the increased number of damage mechanisms found in fibre metal laminates makes their behaviour more difficult to model and predict.

A number of studies have been performed in order to understand the buckling and postbuckling behaviour of fibre composite panels containing delaminations. Numerical investigations on delamination initiation and growth under compressive loading were carried out on slender composite laminates using a finite element (FE) model based on the use of a cohesive element by Wang *et al.* [2]. They concluded that for composite laminates with embedded delaminations the propagation shape is affected by the depth of the delamination, rather than its size. Under an axial compressive load, the damage propagation width was found to expand as the depth increased from 10% to 25% of the total specimen thickness. Mohammadi *et al.* [3] also developed

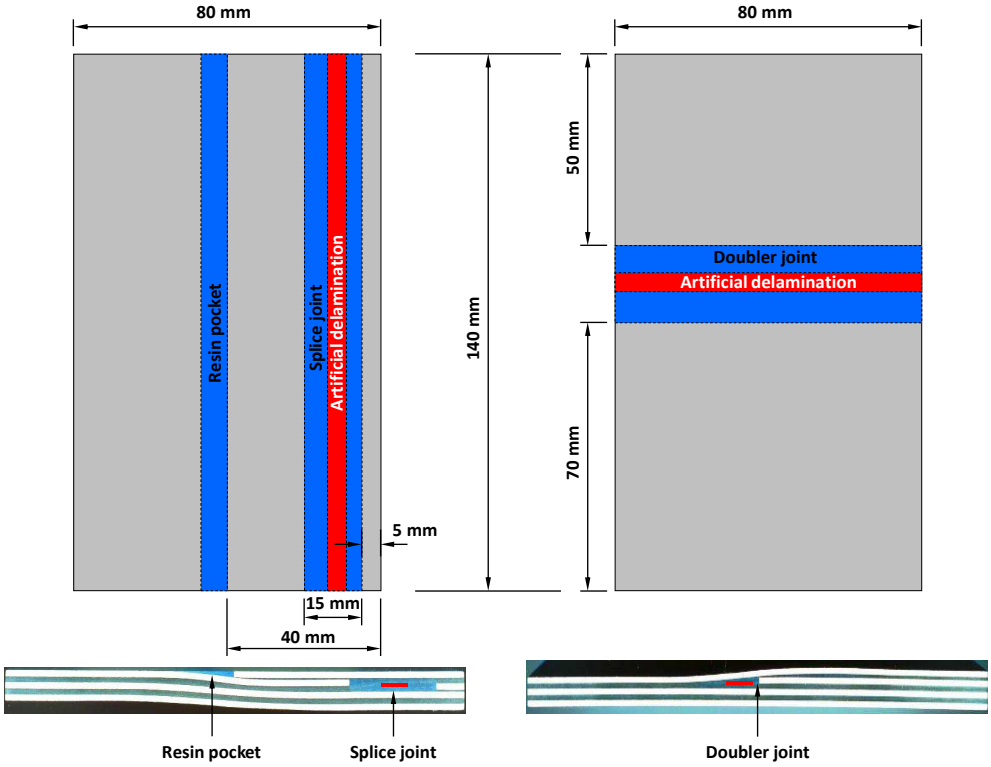

Figure 1: Layout of 'Glare 4B' specimens, (a) longitudinal splice and (b) transverse doubler.

a cohesive element model to predict delamination propagation in laminated composites containing single and multiple through-the-width delaminations during buckling. They found that for specimens with multiple delaminations damage propagation was unstable causing a sudden drop in the load carried accompanied by a global buckling load which was much lower than for a similar specimen with a single delamination. Zhang and Wang [4] developed a B-spline finite strip method to study buckling, postbuckling and delamination propagation in debonded composite laminates under compression. Extensive numerical studies were conducted to validate their theory [5]. Both studies concluded that unstable delamination propagation was often caused by mode-I fracture while mode-II fracture led to stable delamination growth in the cases examined. Chirica and Beznea [6] developed an FE model to predict the buckling behaviour of composite plates with a central elliptical

delamination. They found that the aspect ratio of the delamination had a significant effect on the relationship between in-plane loading and displacement. Akbarov *et al.* [7] developed a three-dimensional model using the theory of viscoelasticity for anisotropic bodies to study delamination around two types of artificial crack (band-crack, edge-crack) introduced into a rectangular plate under compressive loading. They concluded that the mode of buckling delamination around the two types of cracks depended only on the initial infinitesimal imperfection of the edge-surfaces of these cracks. Eaton [8] investigated the propagation of delaminations in simply supported composite panels under compression using an FE model and then validated the results experimentally using acoustic emission to monitor the initiation and propagation of damage. The effect of the inherent mechanical couplings exhibited by fully anisotropic graphite/epoxy laminates on the buckling loads and mode shapes of composite panels were studied by conducting experimental and analytical investigations by Lagace *et al.* [9]. The results indicated that these couplings, especially those relating to stretching and bending behaviour, cause out-of-plane deflections prior to buckling which reduce the buckling load significantly. Further analytical models have been developed [10, 11, 12, 13, 14] enabling the prediction of the compression response of laminated composite panels containing single and multiple delaminations.

In terms of Fibre Metal Laminates less work has been done. Obrzalek and Vrbka [15, 16] performed numerical studies on the buckling of FMLs and concluded that the orientation angle and depth of any delaminations present made a significant difference to their effect on the buckling load which could drop by up to 50%. They also found that the buckling and postbuckling behaviour of the plates was greatly affected by the shape of the delamination.

Geometrical imperfections and load eccentricity have also been shown to have a significant effect on the buckling and postbuckling behaviour of composite laminates. This was confirmed by Hilburger *et al.* [17] who used non-linear analysis to determine accurate, high-fidelity design knock-down factors to be used for predicting composite shell buckling and collapse loads during the design process. Tsouvalis *et al.* [18] investigated the effect of the initial imperfection magnitude on the buckling load of a cylinder under external hydrostatic pressure and found good correlation between experimental and modelling results. Featherston [19] studied the effect of geometrical imperfections on the buckling and postbuckling behaviour of a simple aerofoil under combined shear and in-plane bending, both experimentally and using FE analysis, to determine appropriate knock down factors. Experi-

mental and analytical studies of the effects of initial imperfections on the buckling response and failure of unstiffened thin-walled compression-loaded graphite epoxy cylindrical shells are presented by Hilberger in [20] with results that include the effect of traditional and non-traditional imperfections and uncertainties on the nonlinear response characteristics, buckling loads and failure of the shells included. Eglitis *et al.* [21] performed experimental and numerical studies on the buckling of concentrically and eccentrically compressed composite cylinders. Using knock-down factors estimated from a linear eigenvalue analysis, both experimental and numerical results presented good correlation. Degenhardt *et al.* [22] , Castro *et al.* [23] and Ismail *et al.* [24] developed numerical models for cylindrical shell structures introducing different types of geometrical and load imperfections. Singer *et al.* [25] showed that the buckling and postbuckling behaviour of a rectangular plate depended strongly on both in-plane and out-of plane boundary conditions and that knock-down factors predicted by numerical analyses of the cylinders can be used to account for these effects. For design purposes however, more accurate imperfection values such as experimentally measured geometric imperfections and load eccentricity [21] need to be adopted in order to ensure robust models.

Few researchers have studied the effect of geometrical imperfection and load eccentricity on buckling and postbuckling behaviour of FMLs. Bi *et al.* [26] used an elasto-plastic constitutive model to study the buckling and postbuckling behaviour of FMLs (including Glare®) considering the elasto-plastic deformation of the metal layers. The analysis was implemented using the classical nonlinear plate theory. A simplified three-dimensional rectangular plate model was used and the equations solved using the finite difference method. The effects of initial imperfections in the form of the first eigenmode with different amplitudes (5%, 10% and 15% of the thickness) were numerically investigated. They concluded that by increasing the amplitude of the initial imperfection, the deflection of the plate increased reducing the stiffness prior to buckling. During postbuckling the imperfection had a lesser effect than the plasticity.

This paper focuses on the development of a 3D dynamic explicit FE model generated ply-by ply, directly from detailed scans of real specimens and implemented in the software Abaqus/Explicit to simulate the buckling and postbuckling behaviour of 'Glare 4B' specimens containing splice and doubler features, both with and without artificial defects. By incorporating the full range of damage mechanisms including the use of a cohesive zone model

(CZM) to model delamination initiation and growth under compressive loading, resin and GFRP failure (both matrix and fibre-dominated) and metal plasticity, both bulk material and inter-laminar damage are fully accounted for, providing a unique insight into the behaviour of complex features such as the joints studied here. To make the analysis more representative of as-built structures [27, 28], imperfection sensitivity is also considered: firstly, the effect of geometric imperfections based on the first eigenmode of the specimen (scaled to have a maximum amplitude equal to that measured in the corresponding real specimens) and secondly, load eccentricity which is accounted for by the introduction of an asymmetrical linearly-distributed in-plane displacement component superimposed on the cross-head displacement. To the authors' best knowledge the introduction and study of the effects of these imperfections in the context of a fibre metal laminate joint is unique. Finally, model predictions are verified based on the results of experimental work including Scanning Electron Microscopy (SEM) micrographs which enable the damage found in different areas of the specimen to be characterised for comparison with that predicted by the model. This work, which is summarised here is expanded in [29].

2. Finite Element Models

2.1. Specimen Geometry

Two types of specimens were modelled one incorporating a longitudinal splice and the other a transverse doubler as shown in Figures 2 and 3. Specimens measured 100 mm×80 mm - corresponding to the unsupported section of the 140 mm×80 mm specimens tested for validation. Each had a lay-up type 'Glare 4B' which consists of 0.4 mm thick aluminium alloy 2024-T3 sheets and unidirectional S2-glass/FM94 glass/epoxy GFRP layers. Each of these GFRP 'layers' is in fact a 3-ply sub-laminate with the layup [90°/0°/90°] and a cured ply thickness of 0.133 mm. As shown in Figure 1, artificial delaminations were simulated by introducing 4 mm wide strips of polytetrafluoroethylene (PTFE) film of thickness 10 μm embedded in the splice and doubler structures [29].

2.2. Finite Element Meshes

Three dimensional, ply-by-ply finite element models were generated for both specimen types using the Abaqus/CAE software. The geometry and thickness of each layer were extracted from detailed scans of real specimens

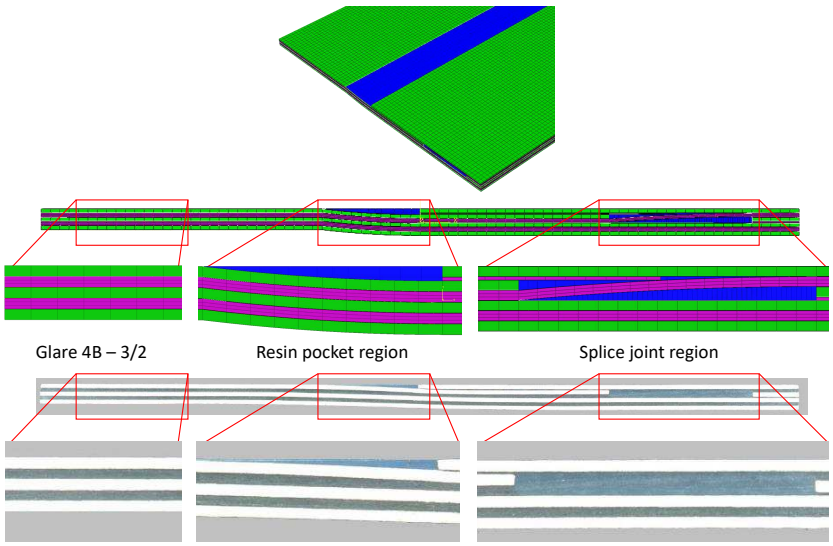

Figure 2: Finite element mesh of the *splice* specimen (top) based on optical scans of real specimens (bottom) (images resized for clarity, not to scale).

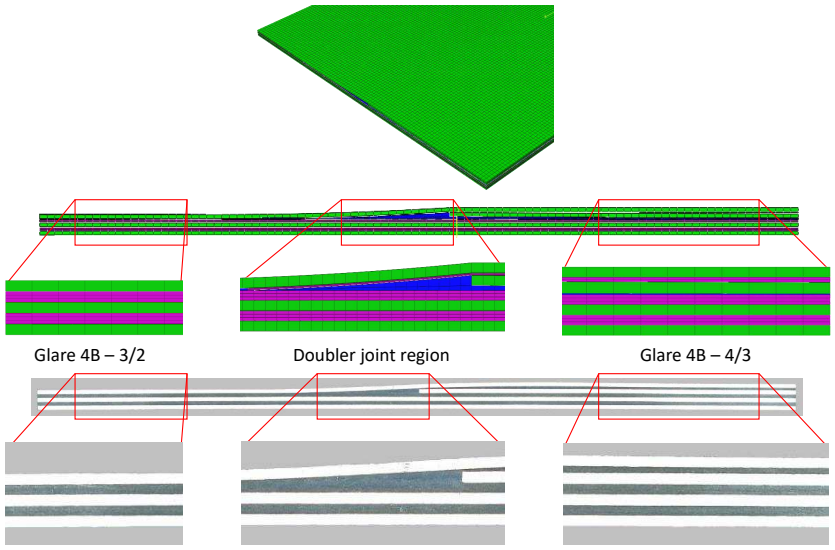

Figure 3: Finite element mesh of the *doubler* specimen (top) based on optical scans of real specimens (bottom) (images resized for clarity, not to scale).

and a high fidelity structural mesh was generated to represent the internal geometry. The resulting meshes are shown in Figures 3 and 2 for doubler

and splice specimens, respectively. The layers of aluminium and the resin pockets were meshed using linear continuum (C3D8R) elements with the interfaces between layers modelled using 0.01 mm thick cohesive (COH3D8) elements (the thickness was chosen based on a review of the literature related to similar models for fibre laminates). Three dimensional 'continuum shell' elements (SC8R), each made of 8 nodes with 3 degrees of freedom (DoF) per node, were used for the composite plies to enable composite damage to be modelled in Abaqus. Individual layers of each of the laminates were meshed separately and then assembled using tie constraints between adjacent layers coupling all nodal degrees of freedom at the interface.

2.3. Material Properties

A comprehensive literature review was conducted on the mechanical properties of the Glare® material constituents. Properties for the aluminium alloy 2024-T3 were obtained from [30] and are summarised in Table 1, with plastic stress-strain behaviour from [31] being presented in Table 2. The mechanical properties for the S2-glass/FM94 GFRP material were given in [32] and are shown in Table 3.

Table 1: Mechanical properties for aluminium alloy 2024-T3 [30].

Property	**Value**	**Units**
Young's modulus	72.4	GPa
Stress at 4.7% strain	420	MPa
Tensile yield strength, rolling direction	347	MPa
Tensile yield strength, transverse direction	299	MPa
Shear modulus	27.6	GPa
Poisson's ratio	0.33	
Coefficient of thermal expansion	22×10^{-6}	$^{\circ}C^{-1}$
Mass density	2780	$kg{\cdot}m^{-3}$

Every interface in the laminate was represented by a Cohesive Zone Model (CZM) with bi-linear traction-separation curves defined independently for modes I and II (further details in Section 2.7). The cohesive properties for GFRP-metal interfaces were obtained from [34] and are shown in Table 4. The cohesive stiffnesses K_{I} and K_{II} were however calculated based on the elastic properties of bulk FM94 resin, shown in Table 5, and the assumption

Table 2: Plastic stress-strain behaviour of aluminium alloy 2024-T3, transverse direction [31].

Plastic strain [%]	**Stress [MPa]**
0.000	300
0.016	320
0.047	340
0.119	355
0.449	375
1.036	390
2.130	410
3.439	430
5.113	450
8.000	470
14.710	484

that the interfacial stiffness is dominated by the deformation of a 10 μm thick resin rich layer, as described in [35] (it should be noted that these stiffnesses have only minor influence on the fracture initiation and propagation behaviour of the CZM, which instead is more strongly dependent on the initiation stresses, $\sigma_{\mathrm{I}}^{\max}$ and $\sigma_{\mathrm{II}}^{\max}$, and critical strain energy release rates, G_{IC} and G_{IIC}).

The fracture process resulting from the delamination of GFRP-metal interfaces is micro-mechanically different from the fracture process observed between the same metal and the same resin in the absence of fibres, since the presence of fibres precludes the development of a local plastic zone within the toughened epoxy material [37]. As a result, much higher fracture energies are expected within the resin pockets formed around the splice and doubler features contained in the laminates investigated here. Indeed, Katnam *et al.* [38] obtained the cohesive properties shown in Table 6 for fracture in a similar material system, but along a 100 μm thick unreinforced resin layer. The properties in Table 6 were therefore assumed for the interfaces formed around resin pockets in the splice and doubler features investigated here.

Finally, artificial delaminations were introduced via a 99.9% reduction in cohesive properties along the interfaces to be covered by the PTFE strip, effectively turning it into a pre-crack. Finally, the bulk PTFE material was modelled using properties taken from the literature and detailed in Table 7.

Table 3: Mechanical properties for S2-glass/FM94 prepreg material [32].

Property	**Value**	**Units**
Youngs modulus, fibre direction, E_{11}	50.0	GPa
Youngs modulus, transverse direction, E_{22}	9.0	GPa
Poissons ratio, ν_{12}	0.33	
Poissons ratio, ν_{23}	0.04	
In-plane shear modulus, G_{12}	3.5	GPa
Transverse shear modulus, G_{13}	3.0	GPa
Fibre-direction tensile strength, X_{T}	2000	MPa
Fibre-direction compressive strength, X_{C}	550	MPa
Transverse tensile strength, Y_{T}	43	MPa
Transverse compressive strength, Y_{C}	90	MPa
In-plane shear strength, S_{12}	93	MPa
Transverse shear strength, S_{23}	50	MPa
Critical SERR*, fibre direction, $G_{\mathrm{C},X}$	12.0	$\mathrm{kJ{\cdot}m^{-2}}$
Critical SERR*, transverse direction, $G_{\mathrm{C},Y}$	1.0	$\mathrm{kJ{\cdot}m^{-2}}$
Mass density, ρ [33]	2000	$\mathrm{kg{\cdot}m^{-3}}$
Coefficient of thermal expansion, fibre direction [30]	6.1×10^{-6}	$^{\circ}\mathrm{C}^{-1}$
Coefficient of thermal expansion, transverse direction [30]	26.2×10^{-6}	$^{\circ}\mathrm{C}^{-1}$

* Strain Energy Release Rate.

Table 4: Cohesive zone properties for GFRP-metal interfaces.

G_{IC} [$\mathrm{kJ{\cdot}m^{-2}}$] [34]	G_{IIC} [$\mathrm{kJ{\cdot}m^{-2}}$] [34]	$\sigma_{\mathrm{I}}^{\max}$ [MPa] [34]	$\sigma_{\mathrm{II}}^{\max}$ [MPa] [34]	K_{I} [$\mathrm{N{\cdot}mm^{-3}}$]	K_{II} [$\mathrm{N{\cdot}mm^{-3}}$]
0.45	1.0	40	40	$2.189{\times}10^5$	$0.823{\times}10^5$

2.4. Loading and Boundary Conditions

Boundary conditions were applied at the top and bottom edges of the specimen corresponding to the effect of the clamps in the validation experiments. The bottom edge was restrained in all three DoFs to represent the fixed end condition, while the top edge was free to move in-plane but restricted in both other DoFs. Both sides of the specimens were left uncon-

Table 5: Mechanical properties for the FM94 resin [36].

Property	**Value**	**Units**
Young's modulus	2.19	GPa
Poissons ratio	0.33	
Mass density	1280	$\mathrm{kg{\cdot}m^{-3}}$
Coefficient of thermal expansion	$1{\times}10^{-4}$	$^{\circ}\mathrm{C}^{-1}$

Table 6: Cohesive zone properties for bulk resin-metal interfaces.

G_{IC} [$\mathrm{kJ{\cdot}m^{-2}}$] [38]	G_{IIC} [$\mathrm{kJ{\cdot}m^{-2}}$] [38]	$\sigma_{\mathrm{I}}^{\mathrm{max}}$ [MPa] [39]	$\sigma_{\mathrm{II}}^{\mathrm{max}}$ [MPa] [39]	K_{I} [$\mathrm{N{\cdot}mm^{-3}}$]	K_{II} [$\mathrm{N{\cdot}mm^{-3}}$]
2.0	4.0	50	50	$2.189{\times}10^{5}$	$0.823{\times}10^{5}$

Table 7: Mechanical properties for the PTFE film [40, 41].

Property	**Value**	**Units**
Young's modulus	480	MPa
Poissons ratio	0.46	
Mass density	2150	$\mathrm{kg{\cdot}m^{-3}}$
Coefficient of thermal expansion	$1{\times}10^{-4}$	$^{\circ}\mathrm{C}^{-1}$

strained as in the validation experiments. An initial Abaqus/Explicit thermal step was implemented to generate the residual stresses created during the curing process based on a curing temperature of 120 °C, and the thermal expansion coefficients shown in Tables 1, 3 and 5. Following this, a compressive load under velocity control was applied to the top edge of the specimen.

2.5. Geometric Imperfections

In order to represent the 'as-built' structures tested in the validation experiments geometric imperfections were introduced. Since their exact form was not known they were modelled in the form of the first mode shape (obtained by performing an eigenmode analysis in Abaqus/standard, Figure 4)

with an amplitude scaled to give a maximum representative of the deviations measured in the specimens tested (due to the manufacturing process and variations in thickness across the specimen).

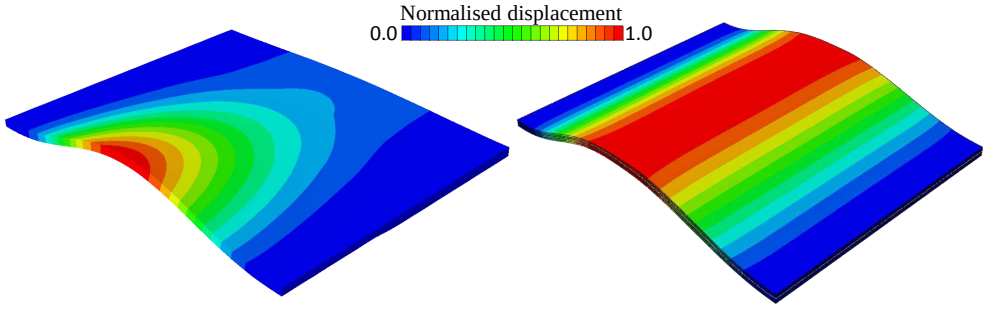

(a) (b)

Figure 4: Geometrical imperfections based on the first eigenmode for (a) splice and (b) doubler specimens (normalised displacements magnified for clarity, not to scale).

2.6. Load Eccentricity

In addition to geometric imperfections, load eccentricity caused by misalignments in clamping the specimen leading to an asymmetrical load distribution was also considered in the analysis. This was achieved by implementing two load steps following the thermal loading step discussed in Section 2.4. As shown in Figure 5 the first step represented the load eccentricity which was introduced in the form of an asymmetric linearly distributed in-plane displacement component superimposed on the cross-head displacement and the second step represented the uniform compression load applied up to the final failure.

2.7. Cohesive Zone Model

As mentioned earlier, one of the complexities of modelling the behaviour of fibre metal laminates is the increased number of damage mechanisms compared to modelling metallic or composite laminates. In order to accurately model the initiation and propagation of damage in the specimens a range of damage and fracture criteria were therefore introduced. The mixed-mode bi-linear cohesive zone model (CZM) shown in Figure 6 was used to model delamination initiation and growth in the metal-fibre and fibre-resin interfaces. This model uses a quadratic nominal stress criterion to identify the

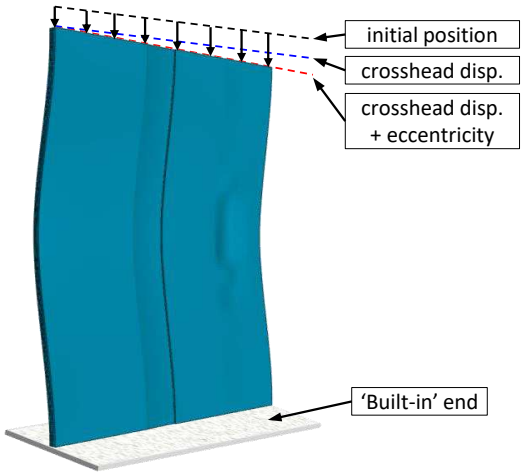

Figure 5: Load eccentricity introduced after the thermal step and before the main loading step.

onset of damage,

$$\left(\frac{\langle\sigma_{\mathrm{I}}\rangle}{\sigma_{\mathrm{I}}^{\max}}\right)^2+\left(\frac{\sigma_{\mathrm{II}}}{\sigma_{\mathrm{II}}^{\max}}\right)^2=1\,, \tag{1}$$

where $\langle\cdot\rangle=\max\left(\cdot\,,0\right)$. Propagation is then based on the strain energy release rates G_{I} and G_{II} for modes I and II respectively,

$$\left(\frac{G_{\mathrm{I}}}{G_{\mathrm{IC}}}\right)^n+\left(\frac{G_{\mathrm{II}}}{G_{\mathrm{IIC}}}\right)^n=1\,. \tag{2}$$

where n is a material-specific power law coefficient. In the absence of reliable mixed-mode fracture data for the various interface types in Glare® , it has been assumed here that $n=1$ so that equation 2 turns into a linear interaction criterion instead [35]. The other interfacial material properties required to completely define the CZMs used in this work are provided in Tables 4 and 6.

2.8. Continuum Damage and Plasticity

Plastic deformation of the aluminium sheets was considered by introducing the stress-strain properties provided in Table 2. The resin pockets were assumed to strain-harden according to the Drucker-Prager yield criterion [42]. A ductile damage criterion was used to model damage in both the aluminium layers and the resin pockets [42]. This criterion assumes that the equivalent

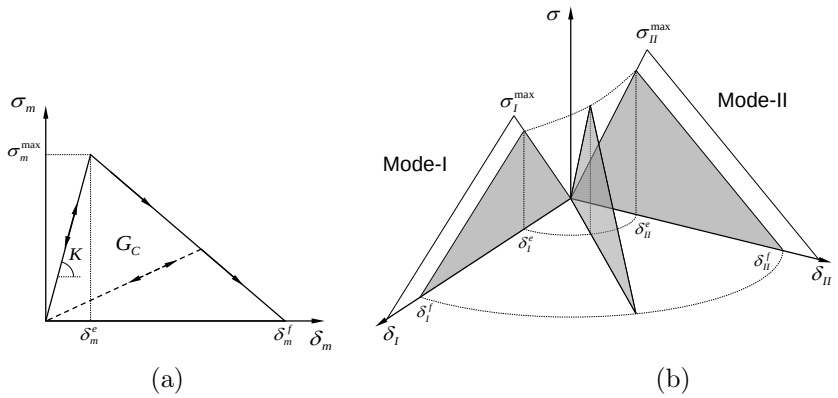

Figure 6: Cohesive Zone Model (CZM) based on bi-linear traction-separation curves (a) which are defined independently for modes I and II (b).

plastic strain at the onset of damage is a function of stress triaxiality and strain rate. The mechanical properties used for both materials are shown in Tables 1 and 5 respectively.

The Hashin damage criterion [43] was used to model damage in the GFRP plies. The model available in the software Abaqus (only applicable to continuum shell elements) is a 2D version of the original Hashin criteria with four damage variables, *i.e.* compressive and tensile failure along the fibre direction and the in-plane transverse direction (for simplicity the former are referred to as 'fibre failure' and the latter 'matrix failure'). The damage initiation criterion for fibre tension is,

$$\left(\frac{\sigma_{11}}{X_{\mathrm{T}}}\right)^2 + \left(\frac{\sigma_{12}}{S_{12}}\right)^2 = 1\,, \tag{3}$$

and for fibre compression,

$$\left(\frac{\sigma_{11}}{X_{\mathrm{C}}}\right)^2 = 1\,, \tag{4}$$

where X_{T} and X_{C} are the fibre-direction tensile and compressive strengths, respectively, and S_{12} is the in-plane shear strength. The initiation criterion for matrix tensile damage is,

$$\left(\frac{\sigma_{22}}{Y_{\mathrm{T}}}\right)^2 + \left(\frac{\sigma_{12}}{S_{12}}\right)^2 = 1\,, \tag{5}$$

and for matrix compressive damage,

$$\left(\frac{\sigma_{22}}{2\,S_{12}}\right)^2 + \left[\left(\frac{Y_{\rm C}}{2\,S_{12}}\right)^2 - 1\right]\frac{\sigma_{22}}{Y_{\rm C}} + \left(\frac{\sigma_{12}}{S_{12}}\right)^2 = 1\,, \tag{6}$$

where $Y_{\rm T}$ and $Y_{\rm C}$ are the transverse direction tensile and compressive strengths respectively.

Once an initiation criterion is satisfied, the evolution of damage variables for each damage mode follows a bilinear stress-displacement curve similar to that of a cohesive formulation (Figure 6a). Integration point strains are converted into displacements via a 'characteristic length' which is based on element dimensions [42]. Three damage variables are tracked, 'fibre damage' $d_{\rm f}$, 'matrix damage' $d_{\rm m}$ and in-plane 'shear damage' $d_{\rm s}$. The 2D stiffness matrix for that integration point then becomes,

$$\mathbf{C}_{\rm d} = \frac{1}{D}\begin{bmatrix} (1-d_{\rm f})\,E_1 & (1-d_{\rm f})(1-d_{\rm m})\,\nu_{21}\,E_1 & 0 \\ (1-d_{\rm f})(1-d_{\rm m})\,\nu_{12}\,E_2 & (1-d_{\rm m})\,E_2 & 0 \\ 0 & 0 & (1-d_{\rm s})\,G\,D \end{bmatrix} \tag{7}$$

where $D = 1 - (1-d_{\rm f})(1-d_{\rm m})\,\nu_{12}\,\nu_{21}$, and the material response at the integration point is given by,

$$\sigma = \mathbf{C}_{\rm d}\,\varepsilon. \tag{8}$$

It should be noted that the damage variables are decomposed into *tensile* and *compressive* damage, *i.e.* $d_{\rm ft}$ and $d_{\rm fc}$ for 'fibre damage' and $d_{\rm mt}$ and $d_{\rm mc}$ for 'matrix damage' respectively.

2.9. Eigenvalue Analyses

Linear eigenvalue analyses were conducted on both types of specimens to provide estimates of the buckling loads and to obtain the eigenmode shapes needed for modelling geometric imperfections. Abaqus/Standard (version 6.12) was used for all of the eigenvalue analyses [42]. An eigenvalue buckling problem finds the loads for which the model stiffness matrix becomes singular. The Lanczos solver is generally faster when a large number of eigenmodes are required for a system with many degrees of freedom, and was therefore used throughout. The output eigenmodes are normalised so that the maximum displacement component is one unit. As mentioned previously, scaled versions of these mode shapes, representative of the size of the amplitude of

imperfections measured in the test specimens were used to model imperfections in the dynamic analyses, since they provide a conservative approach when the exact form of the geometrical imperfections is unknown [42].

2.10. Explicit Dynamic Analysis

As discussed, in order to predict the buckling behaviour of real structures it is important to take into account the various sources of nonlinearity, including plasticity, damage and crack growth. In order to achieve this, the buckling experiments were analysed using the explicit dynamic solver Abaqus/Explicit (version 6.12) [42]. Whilst this software is ideally suited for analysing high-speed dynamic events, it has many advantages for the analysis of slower (quasi-static) processes which are beneficial here. The use of a large number of small time increments in an explicit solution is advantageous because each increment is relatively quick to compute (compared to the direct integration dynamic analysis procedure available in Abaqus/Standard) as it does not require convergence iterations. It also simplifies greatly the treatment of contact. The procedure uses diagonal ('lumped') element mass matrices whose inverses are simple to compute, significantly increasing computational efficiency. In addition, the vector multiplication of the inverse mass matrix by the inertial forces requires only n operations, where n is the number of degrees of freedom in the model. The equations of motion for each node in the domain are integrated using the explicit central-difference integration rule. The explicit procedure requires no global matrix operations and no tangent stiffness matrix calculation [42].

3. Instrumented Tests

In order to validate the models developed here, a series of buckling experiments on specimens containing both splice and doubler joints were conducted. A total of eight specimens were tested, four splice and four doubler, with and without defects (two of each). A specially-designed test rig was used in a servo-hydraulic testing machine as shown in Figure 7. The rig was designed to provide built-in boundary conditions at the upper and lower edges where the specimens were clamped with free boundaries along both sides.

The machine operated under displacement control at a cross-head velocity of 0.1 mm/min. Experiments were monitored using digital image correlation (DIC) and acoustic emission (AE) monitoring. The DIC system provided

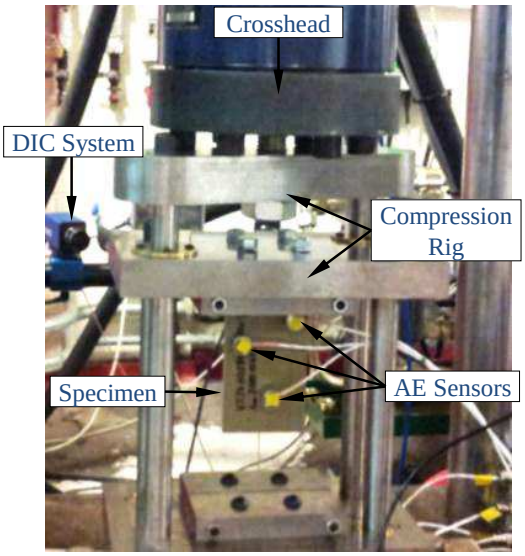

Figure 7: Test setup for the buckling experiments described in [29].

full-field displacement data based on one of the faces of the specimen, while three AE sensors mounted on the opposite face recorded event energies and locations. The latter were computed using the bespoke location algorithm 'Delta T' described in [44], which has been shown to provide greater location accuracy for complex materials and structures such as Glare® laminates [29] than the standard time of arrival techniques normally used. Following testing, specimens were sectioned and inspected using scanning electron microscopy (SEM) to determine the failure modes present. In each case sections were taken both in the area of the joint and remotely (Figures 15 and 24) to allow comparison and hence validation of the damage predictions obtained from the FE models developed. Further details of these experiments are discussed in a companion paper [29].

4. Results and Discussion

A thorough sensitivity study was conducted on the effects of the various sources of nonlinearity described in Section 2 on the behaviour of splice and doubler specimens. The best agreement with experimental results was obtained when all the sources of nonlinearity were included, which suggests that the complex buckling and postbuckling behaviour of such joints is defined by interactions between the various mechanisms. Therefore the results

presented here are for models containing the full set of damage and delamination criteria discussed in Section 2.

4.1. Splice Specimens

Figures 8 and 9 show the displacement behaviour (out-of-plane and in-plane respectively) for splice specimens obtained from the FE models alongside the experimental DIC system data for comparison (specimen 1 of the specimens with defects in Figure 9 suffered from slippage in the rig and has therefore not been considered).

Considering first the out-of-plane displacement, the contour plots presented in Figure 8 illustrate the deformation at initial buckling, peak load and postbuckling, with corresponding in-plane displacements Δx shown separately for model and experiment. Whilst the results presented are for specimens incorporating a defect, the pristine specimens presented very similar behaviour indicating that the effect of the damage introduced on the mode shape and the amplitude of out-of-plane deformations is negligible. The plate is seen to buckle with a single half wave length in the loading direction as expected for a plate with built-in ends and free longitudinal edges under compression. Deformations to the left of the joint in the thinner region of the specimen are higher than those to the right in the thicker region again as would be expected. Good qualitative agreement is observed between experimental and FE results in terms of the mode shape although the FE model underestimates the displacement slightly.

In terms of axial load versus in-plane displacement it can be seen in Figure 9 that in terms of both the pre- and postbuckling stiffness there is a strong correlation between the analytical and experimental results with only a slight overestimation of stiffness in the FE results. In terms of ultimate compressive strengths, the FE model predicted 14.73 kN for both pristine and defective specimens, which overestimates the experimental values of 13.66 kN and 13.50 kN for pristine specimens and 13.86 kN for those containing a defect. This is potentially caused by the use of continuum shell elements which have a simplified treatment of through thickness stresses [45] when modelling the GFRP plies. The effect of the inserted delamination on both pre and postbuckling stiffness and ultimate strength appears to be negligible, possibly due to the relatively small size of the delamination.

The evolution of interface damage is shown in Figure 10 for the critical interface of the splice specimen with the defect with an interface damage value of 1 representing full delamination and a value of zero indicating no

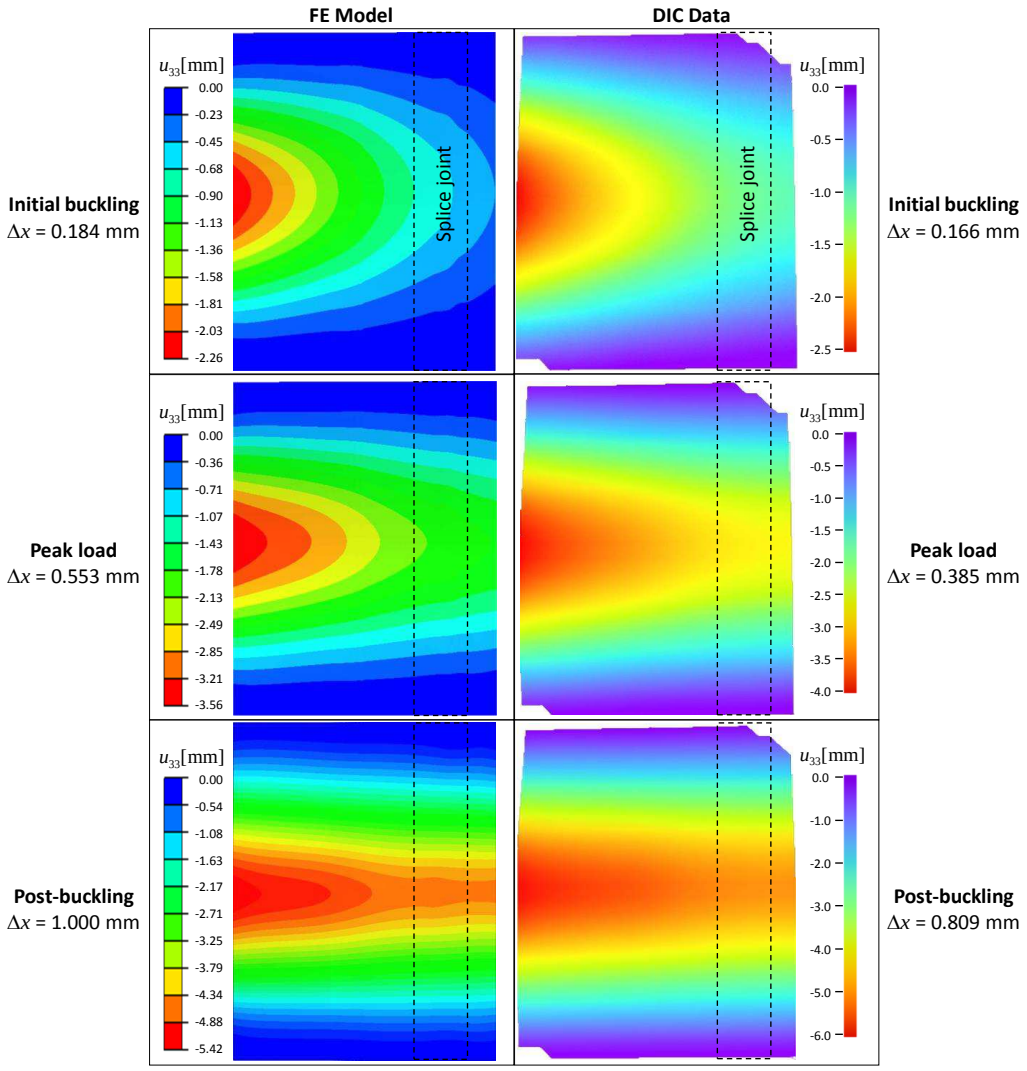

Figure 8: Out-of-plane displacements for the *splice* specimen with an artificial defect; FE predictions and DIC data at different cross-head displacements Δx (dashed line indicates position of splice).

delamination. The results indicate the initiation of interface damage in the area of the splice at initial buckling ($\Delta x = 0.184$ mm) with the delamination propagating throughout buckling and full separation of the splice in the post-buckling region at $\Delta x = 1.0$ mm. Comparison with the AE data in Figure 11 showing the location of cumulative AE events in the specimen supports this

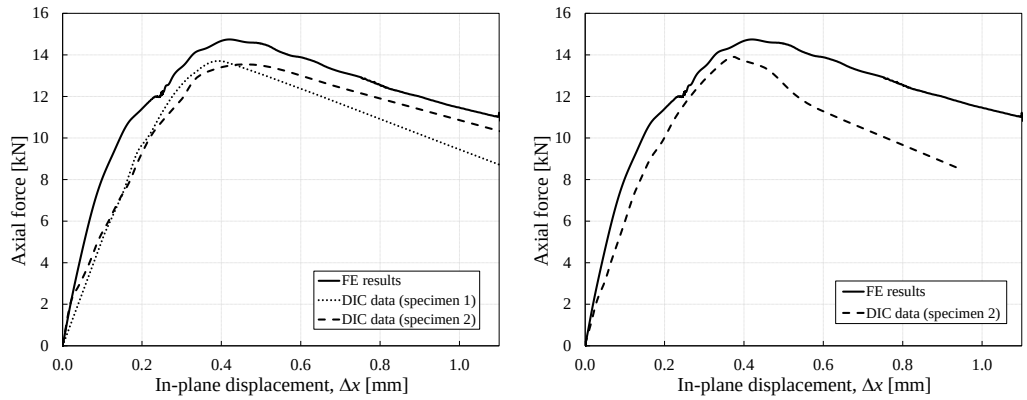

Figure 9: Axial force versus in-plane displacement for *splice* specimens; (a) pristine and (b) with an artificial defect.

prediction with activity seen to initiate in the centre of the splice and propagate along its length as buckling proceeds. Further validation is provided by the SEM micrographs of the splice region (Figure 17) which clearly indicate the presence of matrix cracks leading to delamination in this area. The pristine specimens presented very similar behaviour indicating that the effect of the initial delamination on the interfacial damage is negligible.

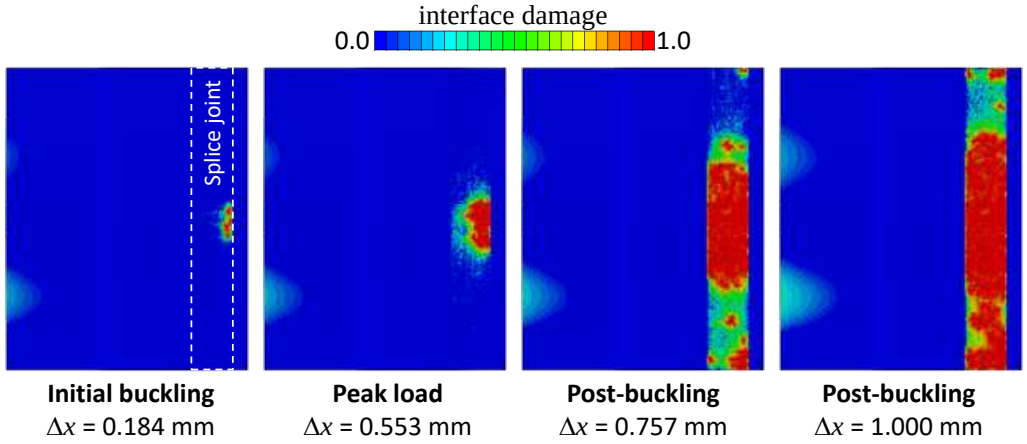

Figure 10: Numerical results for evolution of interface damage along the critical interface in the *splice* specimen with a defect (dashed line indicates position of splice).

In terms of plasticity in the aluminium layers, Figure 12 shows the pre-

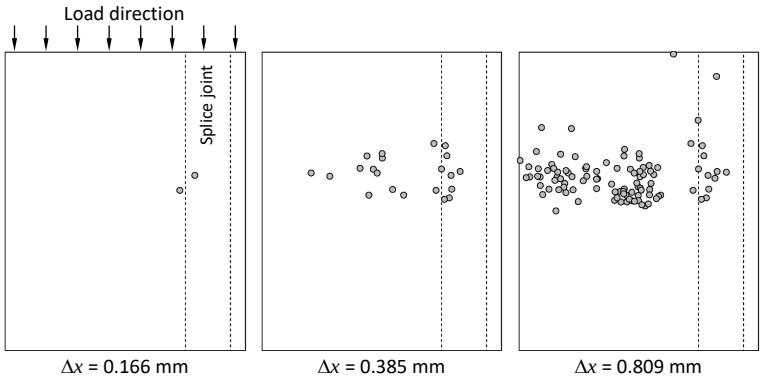

Figure 11: Acoustic Emission event locations in the *splice* specimen at different cross-head displacements Δx (dashed line indicates position of splice); after [29].

dicted plastic strain contours at a cross head displacement $\Delta x = 1$ mm which suggest considerable amounts of energy are being dissipated via plastic deformation of the metallic sheets. Again the result shown is for the specimen with the defect, however the pristine specimens produce very similar behaviour indicating that the effect of this defect on the plasticity of the specimen is negligible. This result is confirmed by both SEM and visual inspection which show large residual curvatures in aluminium layers, in particular near the discontinuity at the joint. This is in direct correlation with the results of the FE model (Figure 12) which predicts higher levels of plastic strain in the joints than in the remainder of the specimen (including the areas of high curvature in the thinner part of the specimen).

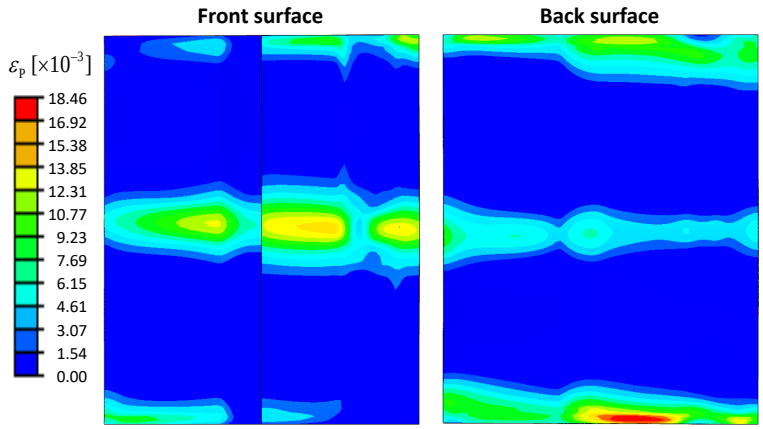

Figure 12: Contours of equivalent plastic strain in the FE model of the *splice* specimen (with an artificial defect) at $\Delta x = 1$ mm.

The evolution of damage in the composite plies is shown in Figure 13 again for the specimen with a defect, with the pristine specimens presenting similar behaviour. As with the interface damage a value of one represents full composite ply damage while a damage value of zero represents no composite damage. The Hashin damage criterion for fibre compression (top of Figure 13) indicates that up to and during critical buckling there is no damage with fibre breakage beginning during postbuckling. This damage is concentrated in the centre of the specimen near the splice joint where the combination of high curvature following buckling and the stress concentration coming from the discontinuity in the aluminium layers creates a weak region. Similar behaviour is noticed for matrix compression (middle of Figure 13) which indicates FE predicted matrix cracking between the fibre layers during postbuckling. Finally, results for matrix shear (bottom of Figure 13) indicate that this occurs during postbuckling. Again peaks can be seen at centre of the specimens particularly in the splice joint for the reasons described above.

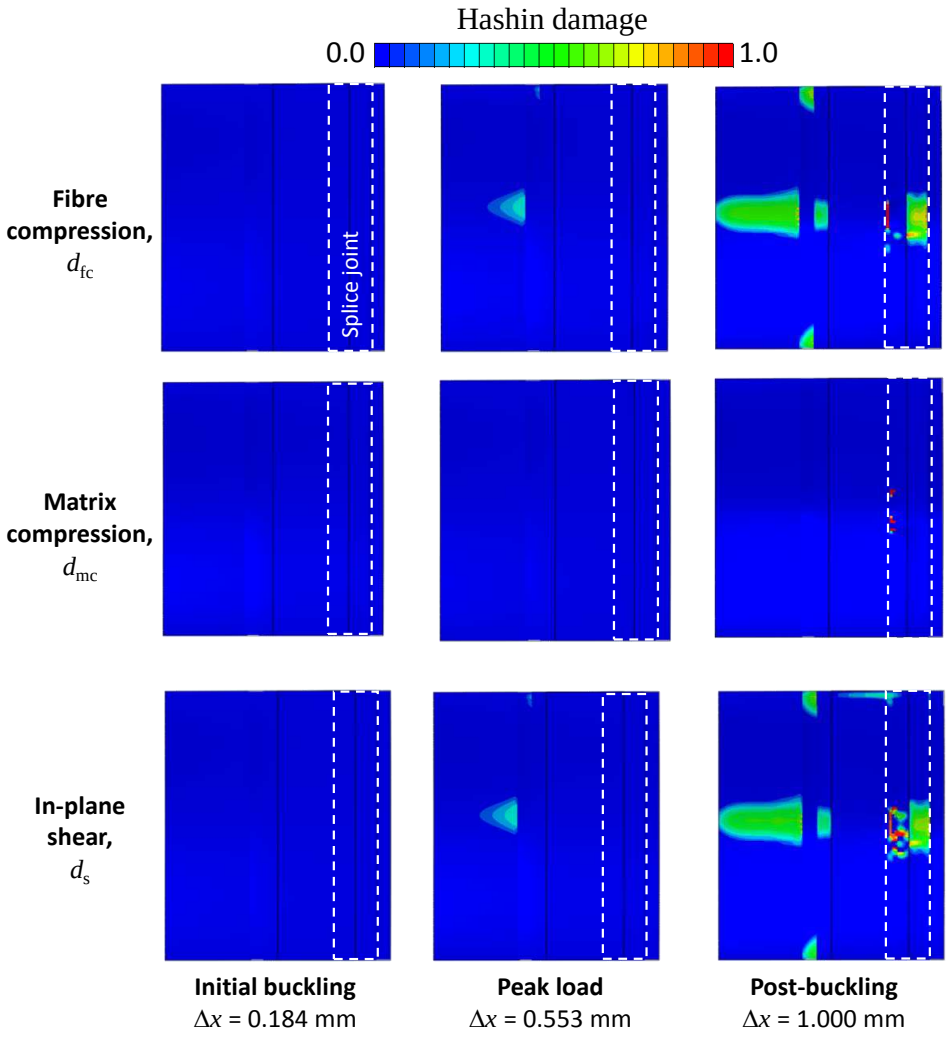

Figure 13: Hashin damage indices for GFRP layers in the *splice* specimen at three different stages of the buckling curve (dashed line indicates position of splice).

The AE data presented in Figure 11 can again be seen to correlate well with the FE predicted damage with a large number of events detected in the centre of the specimen in the area of highest curvature during both buckling and postbuckling, indicating a high level of damage initiation and propagation in this area as predicted by the application of the Hashin criteria. SEM micrographs taken in this region of the panel outside the splice joint (Fig-

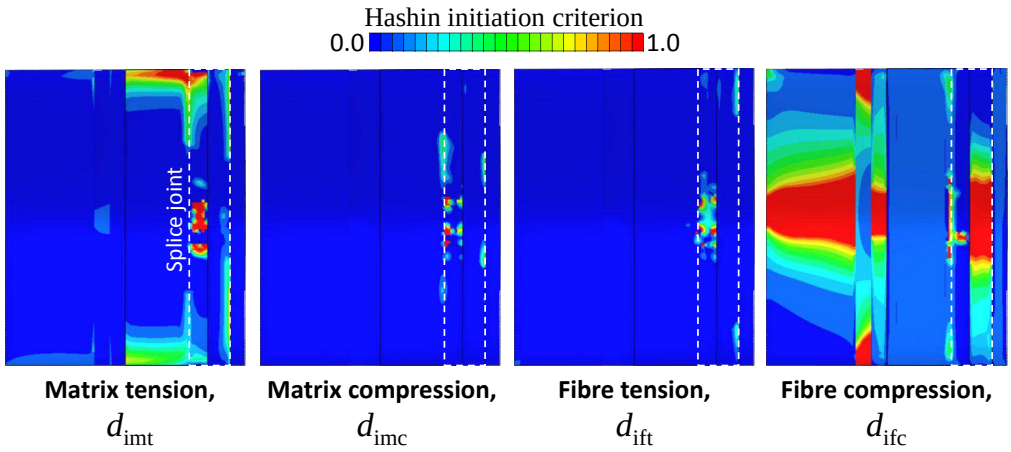

Figure 14: Hashin damage *initiation* variables for the *splice* specimen, at the end of the postbuckling simulation (dashed line indicates position of splice).

ure 16) indicate the presence of matrix cracking in this area, caused by the initiation (Figure 14) and evolution (Figure 13) of damage predicted by the Hashin criteria (with indices of less than one indicating partial damage as discussed in [46]).

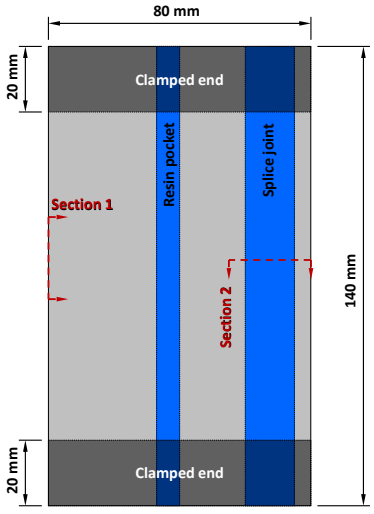

Figure 15: Sections of the *splice* specimen observed under SEM.

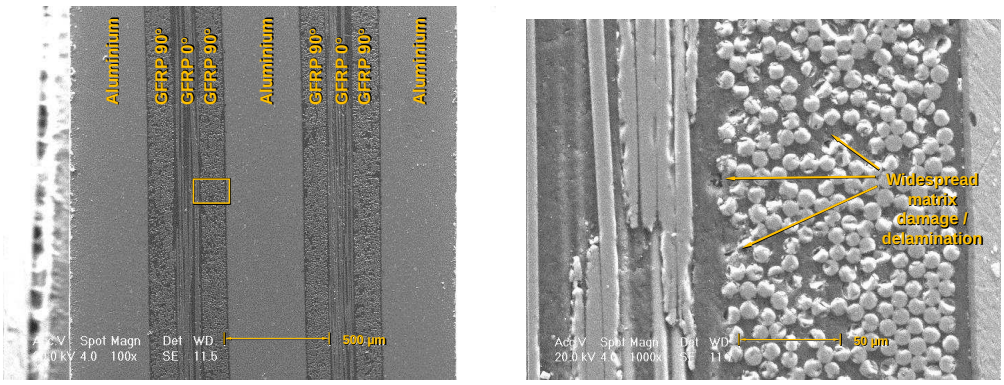

(a) (b)

Figure 16: SEM of *splice* specimens along section 1 (side of specimen), with magnifications of (a) 100× and (b) 1000× (after [29]).

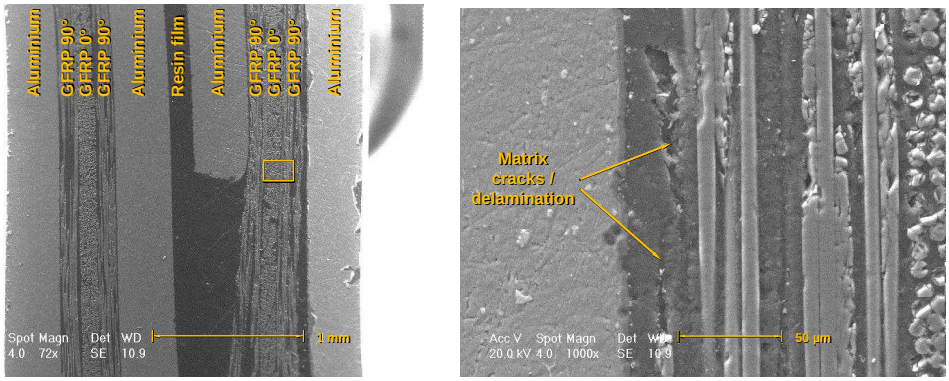

(a) (b)

Figure 17: SEM of *splice* specimens along section 2 (across splice), with magnifications of (a) 72× and (b) 1000× (after [29]).

4.2. Doubler Specimens

For the doubler specimens, Figures 18 and 19 show the out-of-plane and in-plane displacement behaviour obtained from the FE model compared with that from the experimental DIC system data. The out-of plane displacement is shown at initial buckling, peak load and postbuckling, corresponding to in-plane displacements Δx shown separately for model and experiment. The results presented are for specimens incorporating a defect, but the pristine specimens presented very similar behaviour indicating that the effect of the introduced initial delamination on the buckling and postbuckling behaviour is

negligible for the doubler also. The plate is again seen to buckle with a single half wave length in the loading direction as expected. Deformations towards the top of the joint in the thinner region of the specimen are higher than those nearer to the bottom, again as would be expected. Good qualitative agreement is observed between experimental and FE results in terms of the mode shape although the FE model underestimates the displacement slightly.

Axial load versus in-plane displacement for the FE model is compared with that measured during the experimental work in Figure 19. It can be seen that for both the pre and postbuckling stiffnesses there is a strong correlation, with the FE results only slightly overestimating the stiffnesses seen in the experiment. In terms of ultimate compressive strength the FE model predicts a value of 14.89 kN for both pristine and defective specimens whilst experimental values are 13.69 kN and 13.78 kN for pristine specimens and 14.65 kN and 15.49 kN for defected specimens. As mentioned earlier this is believed to be due to the use of shell elements which neglect the through thickness stresses to model the composite layers [45], resulting in an overestimation of their stiffness which is particularly significant in areas of high curvature such as the thinner part of the doubler specimens during postbuckling, while showing very good correlation in elastic and initial buckling regions. In terms of interface damage the model indicated no delamination growth either remote from or within the doubler joint. This is confirmed by the SEM micrographs in Figures 25 and 26.

Figure 20 shows the FE contours of plastic strain for the doubler specimen with a defect at a cross head displacement $\Delta x = 1$ mm. This result is again confirmed by SEM micrographs and visual inspection which show considerable residual curvatures in the aluminium layers, in particular at the ends of the discontinuous layers in the doubler joint. As for the splice model, a considerable amount of energy appears to be dissipated via plastic deformation of the metallic sheets.

The evolution of damage in composite plies is shown in Figure 21 for the doubler specimen with defect with the pristine specimens presenting similar results. The Hashin damage criterion for fibre direction compression (top of Figure 21) indicates that this damage mode initiates during buckling and continues to increase throughout postbuckling with the damage concentrated in the centre of the specimen particularly in the doubler joint as where the highest out-of-plane displacement occurs due to buckling and the discontinuous aluminium layers result in a region of high stress concentration. FE results for transverse direction compression (middle of Figure 21) suggest

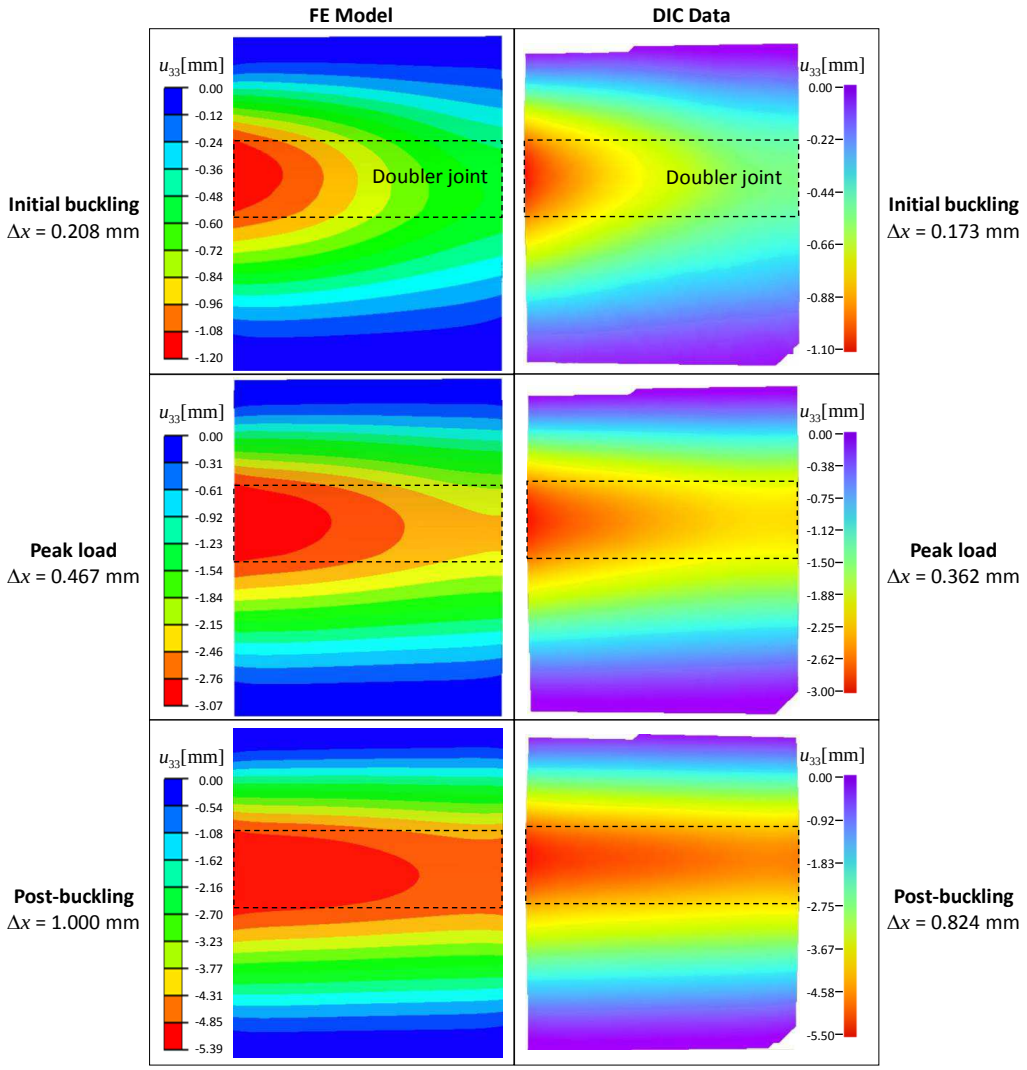

Figure 18: Out-of-plane displacements for the *doubler* specimen with an artificial defect; FE predictions and DIC data at different cross-head displacements Δx (dashed line indicates position of doubler).

that this damage mode initiates between the fibre layers at the left hand side of doubler joint in the critical buckling region and increase during postbuckling to both sides of the doubler joint. Finally, the FE results for matrix shear (bottom of Figure 21) show that this damage mode occurs between the fibre layers at critical buckling and grows during postbuckling in the region

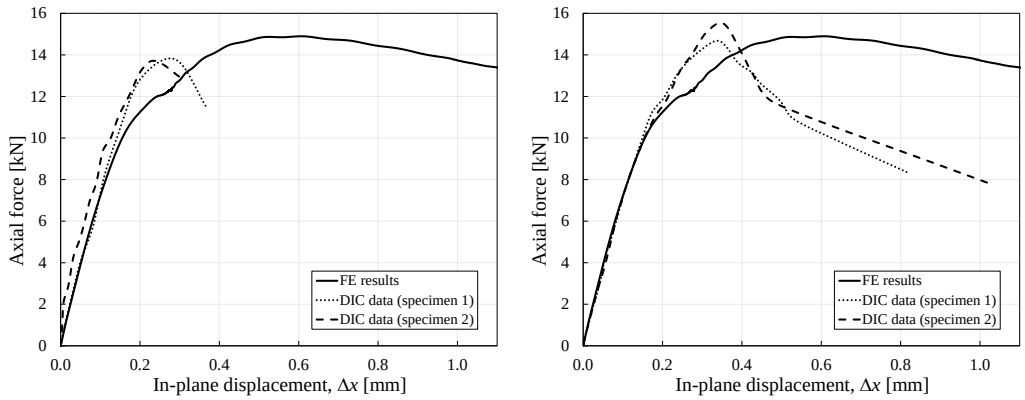

Figure 19: Axial force versus in-plane displacement for *doubler* specimens; (a) pristine and (b) with an artificial defect.

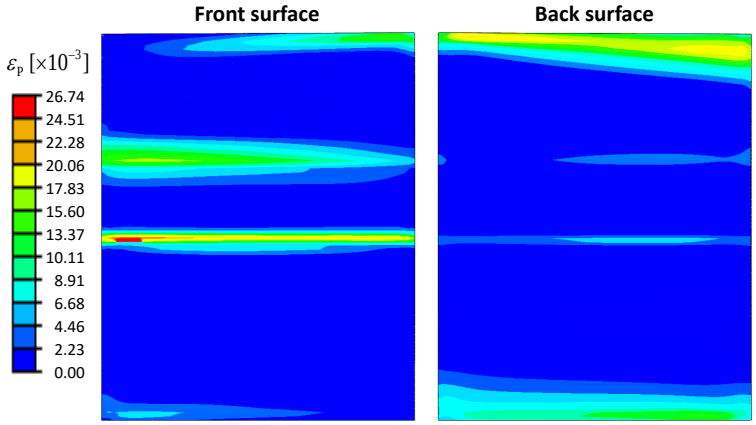

Figure 20: Contours of equivalent plastic strain in the FE model of the *doubler* specimen (with an artificial defect) at $\Delta x = 1$ mm.

of the doubler joint.

The location of the damage predicted using the Hashin criterion is again supported by the AE data shown in Figure 23. It shows a high level of activity in the thinner, upper part of the specimen particularly during postbuckling and up to final failure indicating this is where the majority of damage occurs, thus confirming the capability of the Hashin damage criterion to predict damage in Glare in the buckling and postbuckling regimes. SEM micrographs from this region (Figure 26) indicate that the damage is mostly in the form

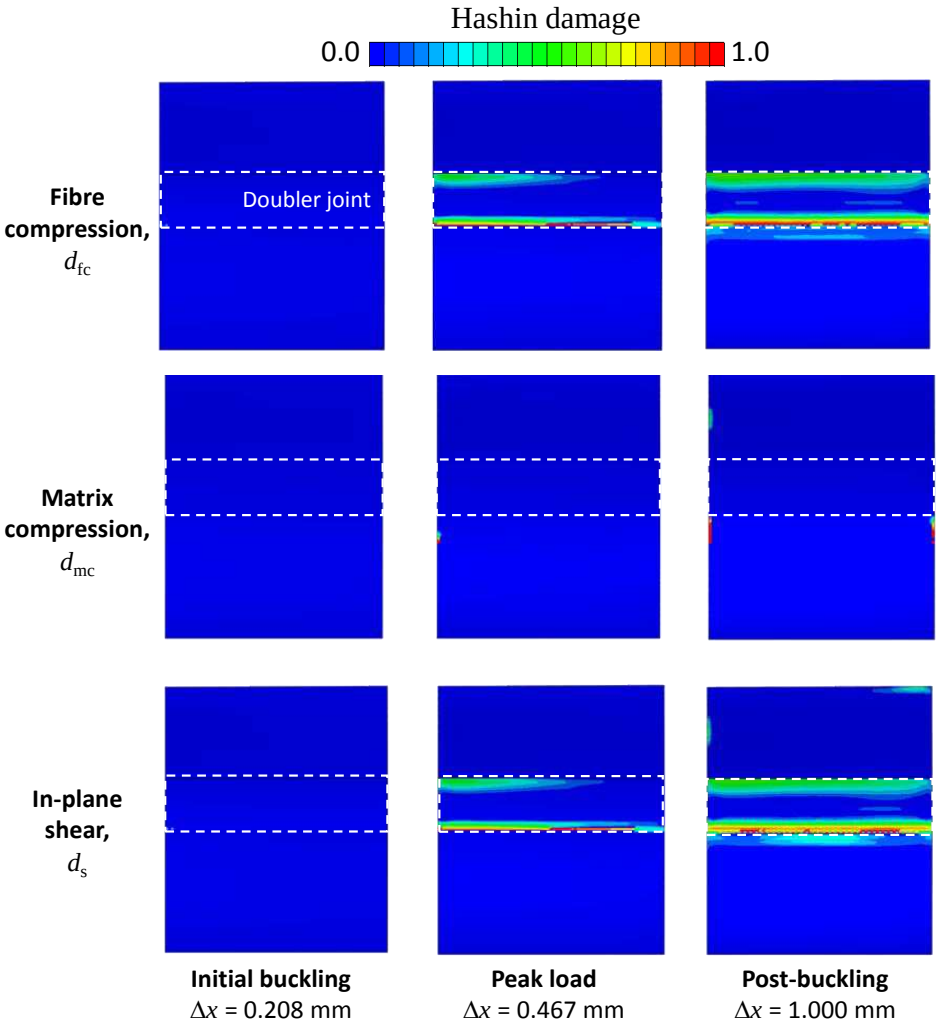

Figure 21: Hashin damage indices for GFRP layers in the *doubler* specimen at three different stages of the buckling curve (dashed line indicates position of doubler).

of matrix cracking as was predicted by the FE model in which the Hashin damage initiation variable for matrix tension (Figure 22) reaches one in this area with lower levels of damage evolution corresponding to in-plane shear (Figure 21).

It should be noted however that the FE model did not predict widespread damage within the thin section as suggested by the AE data, but instead it highlighted damage initiation and evolution *within* the doubler joint and near

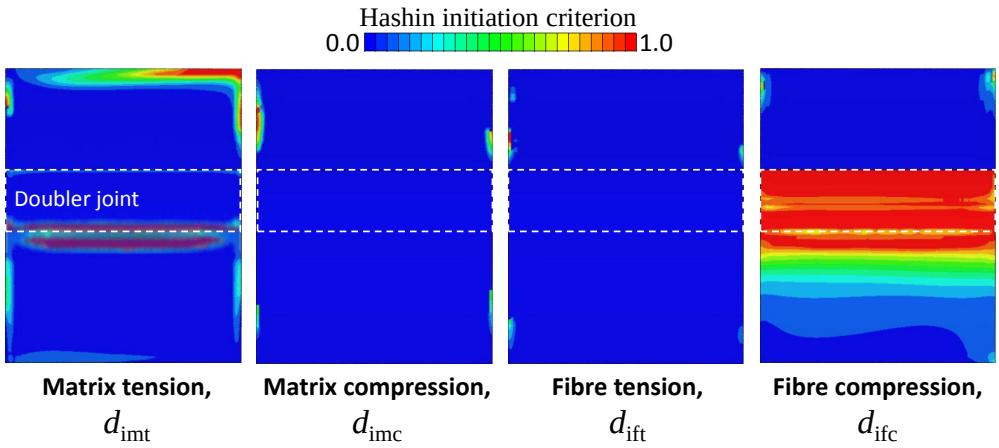

Figure 22: Hashin damage *initiation* variables for the *doubler* specimen, at the end of the postbuckling simulation (dashed line indicates position of doubler).

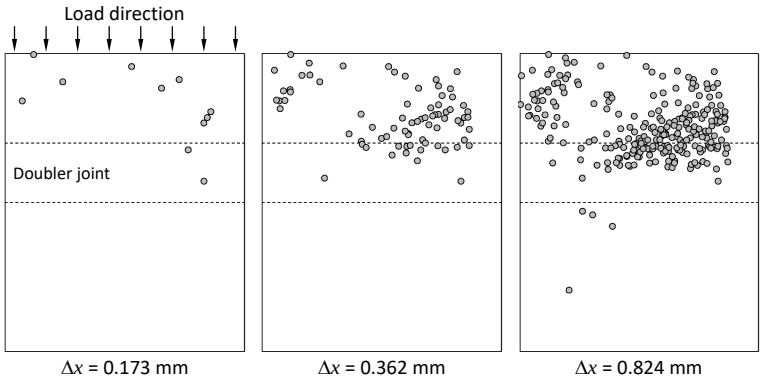

Figure 23: Acoustic Emission event locations in the *doubler* specimen at different cross-head displacements Δx (dashed line indicates position of doubler); after [29].

the upper grip, where local curvatures were high. Possible reasons include local variations in material properties, further geometric imperfections, and the possibility of AE event location being affected by reflections. Future work is required to clarify this issue.

5. Conclusions

Numerical studies to determine the buckling and postbuckling behaviour of Glare® laminates with splice and doubler features showed good agreement

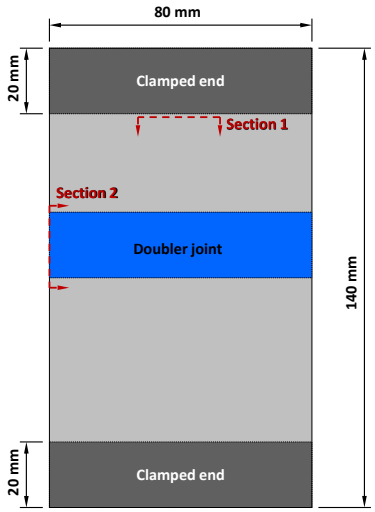

Figure 24: Sections of the *doubler* specimen observed under SEM.

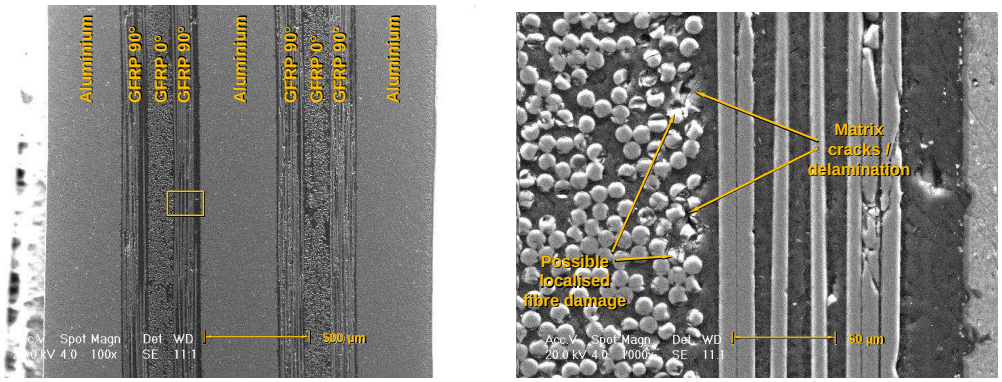

(a) (b)

Figure 25: SEM of *doubler* specimens along section 1 (near the top grip), with magnifications of (a) 100× and (b) 1000× (after [29]).

with experiments in terms of in-plane and out-of-plane displacements thus validating the models used. The gradual evolution of interface damage (delamination) is effectively modelled by a cohesive zone model in the splice joint, which also predicts the lack of delamination in the doubler model. A considerable amount of energy is dissipated via plastic deformation of the metallic sheets in both cases. The FE models predict damage in GFRP layers due mostly to fibre direction and transverse direction compression. In

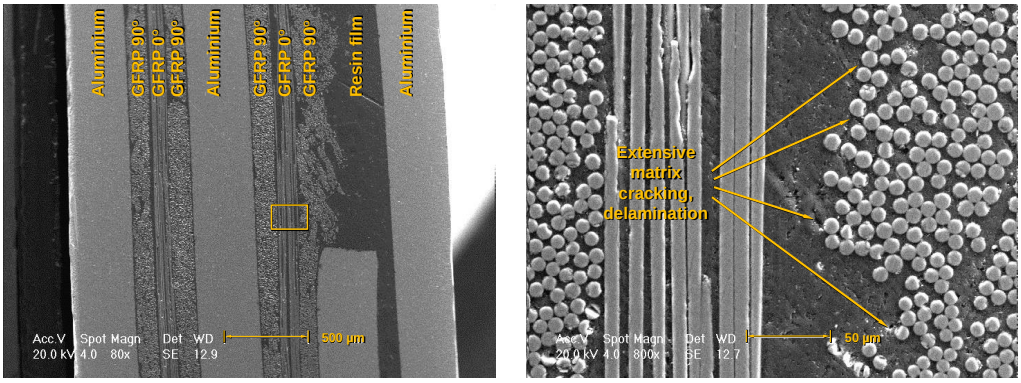

(a) (b)

Figure 26: SEM of *doubler* specimens along section 2 (across doubler), with magnifications of (a) 80× and (b) 800× (after [29]).

addition, delamination between composite plies is observed in both splice and doubler regions. These findings are supported by acoustic emission data collected during validation of experiments. Relatively small embedded artificial delaminations typical of those potentially introduced during manufacturing had a negligible effect on the compressive strength of both splice and doubler specimens, a finding which was also validated by the experimental and numerical results.

6. Acknowledgements

The authors would like to thank Iraqi Ministry of higher education and scientific research for supporting this research, Airbus Germany GmbH for supplying the specimens, and the technical staff of Cardiff School of Engineering for their kind assistance with the testing programme.

7. References

[1] J. W. Gunnink, A. D. Vlot, Fibre Metal Laminates - An Introduction, Kluwer Academic Publishers, 2001. doi:10.1007/978-94-010-0995-9. URL http://www.springer.com/gp/book/9781402000386

[2] R. Wang, L. Zhang, J. Zhang, W. Liu, X. He, Numerical analysis of delamination buckling and growth in slender laminated composite us-

ing cohesive element method, Computational Materials Science 50 (1) (2010) 20–31. doi:10.1016/j.commatsci.2010.07.003.

[3] B. Mohammadi, F. Shahabi, S. Ghannadpour, Post-buckling delamination propagation analysis using interface element with de-cohesive constitutive law, Procedia Engineering 10 (2011) 1797–1802. doi:10.1016/j.proeng.2011.04.299.

[4] Y. Zhang, S. Wang, Buckling, post-buckling and delamination propagation in debonded composite laminates Part 1: Theoretical development, Composite Structures 88 (1) (2009) 121–130. doi:10.1016/j.compstruct.2008.02.013.

[5] S. Wang, Y. Zhang, Buckling, post-buckling and delamination propagation in debonded composite laminates Part 2: Numerical applications, Composite Structures 88 (2009) 131–146.

[6] I. Chirica, E.-F. Beznea, Buckling analysis of the composite plates with delaminations, Computational Materials Science 50 (5) (2011) 1587–1591.

[7] S. Akbarov, N. Yahnioglu, E. Karatas, Buckling delamination of a rectangular plate containing a rectangular crack and made from elastic and viscoelastic composite materials, International Journal of Solids and Structures 47 (25-26) (2010) 3426–3434. doi:10.1016/j.ijsolstr.2010.08.018.

[8] M. Eaton, Acoustic emission (AE) monitoring of buckling and failure in carbon fibre composite structures, Ph.D. thesis, Cardiff University (2007).

[9] P. Lagace, D. Jensen, D. Finch, Buckling of unsymmetric composite laminates, Composite Structures 5 (2) (1986) 101–123.

[10] Z. Kutlu, F.-K. Chang, Composite panels containing multiple through-the-width delaminations and subjected to compression. Part I: Analysis, Composite Structures 31 (1995) 273–296. doi:10.1016/0263-8223(95)00092-5.

[11] H. Suemasu, W. Sasaki, T. Ishikawa, Y. Aoki, A numerical study on compressive behavior of composite plates with multiple circular delaminations considering delamination propagation, Composites Science and Technology 68 (2008) 2562–2567.

[12] W. Wagner, C. Balzani, Prediction of the postbuckling response of composite airframe panels including ply failure, Engineering Fracture Mechanics 77 (2010) 3648–3657.

[13] A. Gupta, B. Patel, Y. Nath, Postbuckling response of composite laminated plates with evolving damage, International Journal of Damage Mechanics 23 (2014) 222–244.

[14] C. Voellmecke, Analytical modelling of nonlinear buckling of (de-) laminated composite struts, PAMM Proc. Appl. Math. Mech. 14 (2014) 201 – 202. doi:10.1002/pamm.201410088.

[15] V. Obdrzalek, J. Vrbka, On buckling of a plate with multiple delaminations, Engineering Mechanics 17 (1) (2010) 37–47.
URL www.engineeringmechanics.cz

[16] V. Obdrzalek, J. Vrbka, On the applicability of simple shapes of delaminations in buckling analyses, Composites Part B: Engineering 42 (3) (2011) 538–545. doi:10.1016/j.compositesb.2010.11.006.

[17] M. Hilburger, J. Starnes, Effects of imperfections on the buckling response of compression-loaded composite shells, International Journal of Non-Linear Mechanics 37 (2002) 623–643. doi:10.1016/S0020-7462(01)00088-9.

[18] N. Tsouvalis, A. Zafeiratou, V. Papazoglou, The effect of geometric imperfections on the buckling behaviour of composite laminated cylinders under external hydrostatic pressure, Composites: Part B 34 (2003) 217–226.

[19] C. A. Featherston, Experimental buckling of a simple aerofoil under combined shear and in-plane bending, Journal of Mechanical Engineering Science 218 (2) (2004) 155–172. doi:10.1243/095440604322886919.

[20] M. Hilburger, J. Starnes, Effects of imperfections of the buckling response of composite shells, Thin-Walled Structures 42 (2004) 369–397.

[21] E. Eglitis, K. Kalnins, O. Ozolinsh, The influence of loading eccentricity on the buckling of axially compressed imperfect composite cylinders, Mechanics of Composite Materials 46 (5) (2010) 483–492.
URL http://dx.doi.org/10.1007/s11029-010-9165-7

[22] R. Degenhardt, A. Kling, A. Bethge, J. Orf, L. Krger, R. Zimmermann, K. Rohwer, A. Calvi, Investigations on imperfection sensitivity and deduction of improved knock-down factors for unstiffened CFRP cylindrical shells, Composite Structures 92 (2010) 1939–1946.

[23] S. Castro, R. Zimmermann, M. A. Arbelo, R. Khakimova, M. Hilburger, R. Degenhardt, Geometric imperfections and lower-bound methods used to calculate knock-down factors for axially compressed composite cylindrical shells, Thin-Walled Structures 74 (2014) 118–132.

[24] M. Ismail, J. Purbolaksono, A. Andriyana, C. Tanb, N. Muhammad, H. Liew, The use of initial imperfection approach in design process and buckling failure evaluation of axially compressed composite cylindrical shells, Engineering Failure Analysis 51 (2015) 20–28.

[25] J. Singer, J. Arbocz, T. Weller, Buckling Experiments, Experimental Methods in Buckling of Thin-Walled Structures, Vol. 2, John Wiley and Sons, 2002.

[26] R. Bi, Y. Fu, Y. Tian, C. Jiang, Buckling and postbuckling analysis of elasto-plastic fiber metal laminates, Acta Mechanica Solida Sinica 27 (1) (2014) 73–84.

[27] J. Remmers, R. de Borst, Delamination buckling of fibre-metal laminates, Composites Science and Technology 61 (2001) 2207–2213. doi:10.1016/S0266-3538(01)00114-2.

[28] S. Novoselac, T. Ergic, P. Balicevic, Linear and nonlinear buckling and post buckling analysis of a bar with the influence of imperfections, Tehnicki vjesnik 19 (3) (2012) 695–701.

[29] A. Al-Azzawi, J. McCrory, L. Kawashita, C. Featherston, R. Pullin, K. Holford, Buckling and post-buckling behaviour of glare laminates containing splices and doublers. Part 1: Instrumented tests, (*manuscript submitted to* Composite Structures).

[30] R. Alderliesten, Fatigue crack propagation and delamination growth in glare, Ph.D. thesis, Delft University of Technology (2005).
URL http://resolver.tudelft.nl/uuid:15006e44-1232-4ef2-87bd-776b249d61f5

[31] P. Linde, J. Pleitner, H. de Boer, C. Carmone, Modelling and simulation of fibre metal laminates, in: Abaqus Users Conference, Boston, Massachusetts, 25-27 May, 2004.
URL www.simulia.com/forms/world/pdf2004/LINDE.pdf

[32] S. Sugiman, A. Crocombe, The static and fatigue response of metal laminate and hybrid fibre-metal laminate doublers joints under tension loading, Composite Structures 94 (2012) 2937–2951.

[33] A. Seyed-Yaghoubi, B. Liaw, Experimental and numerical approaches on behavior of Glare 5 beams: Influences of thickness and stacking sequence, in: R. Allemang, J. D. Clerck, C. Niezrecki, J. Blough (Eds.), Topics in Modal Analysis II, Volume 6: Proceedings of the 30th IMAC, Springer New York, 2012, pp. 7–16. doi:10.1007/978-1-4614-2419-2_2.

[34] P. Naghipour, K. Schulze, J. Hausmann, M. Bartsch, Numerical and experimental investigation on lap shear fracture of Al/CFRP laminates, Composites Science and Technology 72 (2012) 1718–1724. doi:10.1016/j.compscitech.2012.07.012.

[35] L. F. Kawashita, S. R. Hallett, A crack tip tracking algorithm for cohesive interface element analysis of fatigue delamination propagation in composite materials, International Journal of Solids and Structures 49 (2012) 2898–2913.

[36] Cytec, FM 94 Adhesive film technical data sheet (2010).
URL https://cytec.com/sites/default/files/datasheets/FM_94_032910.pdf

[37] L. Kawashita, A. Kinloch, D. Moore, J. Williams, The influence of bond line thickness and peel arm thickness on adhesive fracture toughness of rubber toughened epoxyaluminium alloy laminates, International Journal of Adhesion & Adhesives 28 (2008) 199–210.

[38] K. Katnam, A. Crocombe, H. Sugiman, H. Khoramishad, I. Ashcroft, Static and fatigue failures of adhesively bonded laminate joints in moist environments, International Journal of Damage Mechanics 20 (2011) 1217–1242. doi:10.1177/1056789510395363.

[39] V. Rooijen, Bearing strength characteristics of standard and steel reinforced Glare®, Ph.D. thesis, Delft University of Technology (2006).

[40] DuPont, PFA Fluorocarbon film properties bulletin (H-04321-4) (2004). URL http://www2.dupont.com/Teflon_Industrial/en_US/assets/downloads/h04321.pdf

[41] DuPont, Teflon® Fluoropolymer resin properties handbook (H-37051-3) (2004).

[42] Dassault Systemes, Abaqus analysis user's manual version 6.12 (2012). URL http://www.3ds.com/products-services/simulia/products/3dexperience/

[43] Z. Hashin, Failure criteria for unidirectional fibre composites, ASME Journal of Applied Mechanics 47 (2) (1980) 329–334.

[44] M. Baxter, R. Pullin, K. Holford, S. Evans, Delta T source location for acoustic emission, Mechanical Systems and Signal Processing 21 (2007) 1512–1520. doi:10.1016/j.ymssp.2006.05.003.

[45] G. Mohamed, Modelling damage and fracture of fibre metal laminates subject to blast loading, Ph.D. thesis, University of Sheffield (2012).

[46] G. S. Makandar, N. K. Chhapkhane, S. Sawant, Progressive failure analysis of compression-loaded composite flat panel with cutout, International Journal on Theoretical and Applied Research in Mechanical Engineering (IJTARME) 3 (2) (2014) 2319–3182.